A Dense Reference Network for Mass-Market Centimeter-Accurate Positioning

Matthew J. Murrian, Collin W. Gonzalez, and Todd E. Humphreys
Aerospace Engineering and Engineering Mechanics
The University of Texas at Austin
Austin, TX, 78712–1221
Email: matthew.murrian@utexas.edu

Thomas D. Novlan
Samsung Research America
Dallas, TX
Email: t.novlan@samsung.com

***Abstract*—The quality of atmospheric corrections provided by a dense reference network for centimeter-accurate carrier-phase differential GNSS (CDGNSS) positioning is investigated. A dense reference network (less than 20 km inter-station distance) offers significant benefits for mass-market users, enabling low-cost (including single-frequency) CDGNSS positioning with rapid integer ambiguity resolution. Precise positioning on a mass-market platform would significantly influence the world economy, ushering in a host of consumer-focused applications such as globally-registered augmented and virtual reality and improved all-weather safety and efficiency for intelligent transportation systems, applications which have so far been hampered by the several-meter-level errors in standard GNSS positioning. This contribution examines CDGNSS integer ambiguity resolution performance in terms of network correction uncertainty, and network correction uncertainty, in turn, in terms of network density. It considers the total error in network corrections: a sum of ionospheric, tropospheric, and reference station multipath components. The paper's primary goal is to identify the network density beyond which mass-market users would see no further significant improvement in ambiguity resolution performance. It finishes by describing development and deployment of a low-cost dense reference network in Austin, Texas.**

***Keywords*—carrier-phase positioning, GNSS reference networks, multipath mitigation**

I. Introduction

There is evidence of strong demand for low-cost precise positioning in the mass market. Carrier-phase differential GNSS (CDGNSS) positioning, which is accurate to within a few centimeters even on a moving platform, would satisfy this demand were its cost significantly reduced. Low-cost CDGNSS can be viewed as a key enabler for consumer applications ranging from virtual and augmented reality to 3D mapping to all-weather positioning for automated vehicles.

Centimeter-accurate positioning by CDGNSS is not new; the technique has been perfected over the past two decades for applications in geodesy, precision agriculture, surveying, and machine control. But mass market use of precise positioning will demand much lower user cost than any current application, yet still require rapid and accurate position fixing. Existing CDGNSS-capable receivers range in cost from $500 to more than $5,000, and a subscription for the correction data on which they depend ranges from $300 to $1500 per annum. Widespread adoption of precise GNSS positioning technology will require a radical cost reduction—by a factor of 10 to 100. To achieve this, mass-market CDGNSS-capable receivers will have to make do with inexpensive, low-quality antennas whose multipath rejection and phase center stability are inferior to those of antennas typically used for CDGNSS. Moreover, to keep costs low, there will be a strong incentive for mass-market CDGNSS-capable receivers to be single frequency, whereas almost all receivers used for CDGNSS in surveying, etc., are multi-frequency. Despite these user-side disadvantages, mass-market precise positioning will be expected to demonstrate convergence and accuracy performance rivaling that of the most demanding current precise positioning applications: impatient mass-market users will be unsatisfied with techniques requiring more than a few tens of seconds to converge to a reliable sub-decimeter solution.

Meeting this challenge calls for bold innovation on both the user (rover receiver) side and on the reference network side of precise satellite positioning. There is currently great interest in user-side techniques for reducing the effects of multipath and speeding convergence time despite poor antennas [1]–[4]. This paper examines the challenge of mass-market precise positioning from the point of view of the reference network. It asks "How should the reference network be designed to support use of low-cost rover receivers while minimizing convergence time to an accurate and reliable fix?"

Over the past decade, the trend in precise satellite-based positioning has been toward the so-called precise point positioning (PPP) technique, whose primary virtue is the sparsity of its reference network. But standard PPP requires several tens of minutes or more to converge to a sub-10-centimeter 95% horizontal accuracy [5]–[7]. Sub-decimeter accuracy is an appropriate target for consumer applications such as lane departure warning. To be sure, the convergence time of standard PPP will decrease with the introduction of new GNSS constellations and signals. But early results indicate that augmenting GPS with a full complement of multi-frequency BDS and GLONASS signals only offers a modest reduction in convergence time [8]. Standard PPP convergence time is therefore unlikely to fall below 5 minutes, which is unacceptably long for the majority of mass-market applications.

Faster convergence can be achieved by re-casting the PPP problem as one of relative positioning, thereby exposing integer ambiguities to the end user. This technique, known as

Preprint of the 2016 IEEE/ION PLANS Conference Savannah, GA, April 11–14, 2016

PPP-RTK or PPP-AR, is mathematically similar to traditional network real-time kinematic (NRTK) positioning [9]. As the network density is increased, sub-minute or even instantaneous convergence is possible with dual-frequency high-quality receivers [6]. Even single-frequency PPP-RTK is possible, with convergence times of approximately 5 minutes for a 40-km network spacing [10].

For PPP-RTK and NRTK, convergence time is synonymous with the time required to resolve the integer ambiguities that arise in the double-difference (DD) carrier-phase measurements, referred to in this paper as time to ambiguity resolution, or TAR. As reference networks become denser, they are better able to compensate for the spatially-correlated variations in signal delay introduced by irregularities in the ionosphere and, to a lesser extent, in the neutral atmosphere [6], [7]. The improvement is manifest as reduced uncertainty in the atmospheric corrections that the network sends to the user. Reduced uncertainty in the atmospheric corrections is key to reducing TAR [11].

Prior work has established an analytical connection between uncertainty in the ionospheric corrections, denoted σ_ι, and TAR, beginning with the introduction of the ionosphere-weighted model in [11] and culminating in the analytical formulations for so-called Ambiguity Dilution of Precision (ADOP) in [12]. ADOP can be used to accurately predict the probability $P(\hat{\boldsymbol{z}} = \boldsymbol{z})$ that the vector of estimated integer ambiguities $\hat{\boldsymbol{z}}$ is equal to the vector of true ambiguities $\boldsymbol{z}$. TAR can be defined as the time required for $P(\hat{\boldsymbol{z}} = \boldsymbol{z})$ to rise above a specified value (e.g., 0.99), or, equivalently, for ADOP to fall below a specified value (e.g., 0.12 cycles).

The existing literature does not, however, offer a satisfactory model for the dependence of σ_ι on network density. The prevailing model, adopted in [13] and [11], is based on single-baseline CDGNSS, which is inapt for PPP-RTK and NRTK. Moreover, prior work does not address the effect of network-side multipath on the accuracy of the corrections data, which becomes increasingly important as low-cost and poorly-sited reference stations are used to densify the network.

This paper makes four primary contributions. First, it presents a compact summary of the functional relationship between σ_ι and $P(\hat{\boldsymbol{z}} = \boldsymbol{z})$ for single- and dual-frequency CDGNSS in scenarios representative of mass-market positioning. Second, it develops a simple analytical model that relates the variance of errors in network-provided corrections to network density. The model highlights the ability of dense networks to suppress network-side multipath by applying a strong linear model for atmospheric delays. Third, it presents the results of a thorough empirical investigation of the relationship between network density and the total uncertainty in network correction data. The key result of this investigation is a plot revealing the network density beyond which users will experience no further significant improvement in ambiguity resolution performance. Finally, the paper describes the design of a low-cost dense reference network being deployed in Austin, Texas.

II. Ambiguity Resolution Performance as a function of ionospheric uncertainty

Reducing the ionospheric uncertainty σ_ι allows a strong prior constraint to be applied in the ionosphere-weighted model, thereby increasing $P(\hat{\boldsymbol{z}} = \boldsymbol{z})$ [11]. It is instructive to consider $P(\hat{\boldsymbol{z}} = \boldsymbol{z})$ for *single-epoch* ambiguity resolution (AR). This is true for two reasons. First, for stationary users with low-cost equipment, multipath errors dominate in the carrier-phase measurement and are strongly correlated over 100 seconds or more [3]. Thus, if single-epoch AR fails then a static user may have to wait an unacceptably long time for multipath errors to decorrelate enough to permit AR. In any case, singe-epoch performance is a strong predictor of multi-epoch performance over an interval short enough (a few tens of seconds) to satisfy impatient mass-market users.

The second reason for considering single-epoch AR is the existence of a convenient and accurate analytical model for single-epoch AR that reveals the dependency of ADOP, and, by extension, $P(\hat{\boldsymbol{z}} = \boldsymbol{z})$, on scenario parameters of practical interest. This model, presented in [12] and [14], relates ADOP to the following parameters: the standard deviation of ionospheric correction errors σ_ι, the number of visible satellites m, the standard deviation of undifferenced carrier- and code-phase measurement errors, σ_ϕ and σ_ρ, respectively, (including multipath-induced errors), a satellite geometry factor f_g, the number p of free parameters to be estimated ($p = 3$ for negligible tropospheric error, $p = 4$ to estimate a single additional tropospheric parameter), and the number of carrier frequencies broadcast by each of the m satellites (e.g., 1, 2, or 3) along with each carrier's wavelength. The model is highly accurate for single-epoch AR, but only approximate for multiple epochs, with accuracy degrading as the data interval lengthens. The model's inaccuracy results from its assumption that overhead satellites remain static from epoch to epoch, which yields pessimistic results for even fairly short data capture intervals (e.g., 30 seconds) [3]. Fully accounting for satellite motion in an analytical model for ADOP is an open problem (presently intractable), which is why ADOP studies that wish to account for satellite motion resort to simulation [3].

In [14] the analytical ADOP model was applied, together with a simulation study, to conclude that single-frequency CDGNSS positioning would be possible over baselines up to 10-15 km if signals from full constellations of both GPS and Galileo were exploited. These conclusions are, however, based on optimistic scenario parameters that would be unrealistic for low-cost rover receivers in mass-market applications. In particular, the authors assume $\sigma_\phi = 2$ mm, $\sigma_\rho = 20$ cm, and an elevation mask angle of 10 degrees, which would only be appropriate for a survey-grade antenna in a low multipath environment with a clear view of the sky. For a low-quality patch antenna, such as would be appropriate for a mass-market receiver, and a moderate multipath environment, $\sigma_\phi = 2.75$ mm is more realistic (see Fig. [4] in [15], dividing the 5.5 mm ensemble standard deviation by two to obtain the

undifferenced σ_ϕ). In adverse multipath, which is common in mass-market applications, σ_ϕ can be expected to be 3 mm or higher. A shift from $\sigma_\phi = 2$ mm to $\sigma_\phi = 3$ mm may not appear significant, but in fact ADOP is highly sensitive to σ_ϕ, so realistic values for σ_ϕ are crucial for accurate projections of ADOP.

Similarly, the value $\sigma_\rho = 20$ cm is unrealistic for low-cost receivers, even for benign multipath environments, and an elevation cutoff angle of 15 to 30 degrees would be more appropriate.

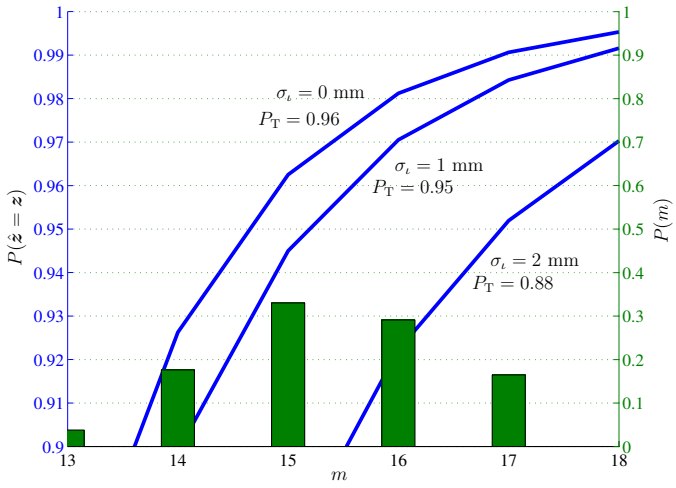

Fig. 1. Single-epoch single-frequency ambiguity fixing. Blue traces (left axis) indicate the probability $P(\hat{z} = z)$ of correctly resolving all integer ambiguities with a single epoch of data as a function of the number of satellites m. Each trace represents $P(\hat{z} = z)$ for a different value of ionospheric uncertainty σ_ι. Green bars (right axis) represent the probability mass function $P(m)$ for the number of satellites above an elevation mask angle of 15 degrees, assuming 31 GPS, 14 Galileo, and 3 WAAS satellites, which corresponds to the projected constellations in late 2018. Each blue trace is marked with the total probability of correct integer resolution P_T, which is a function of both the trace itself and $P(m)$. Other parameters of the scenario are as follows: geometry factor $f_g = 2.5$, standard deviation of undifferenced phase measurements $\sigma_\phi = 3$ mm, standard deviation of undifferenced pseudorange measurements $\sigma_\rho = 50$ cm, and number of estimated parameters $p = 3$.

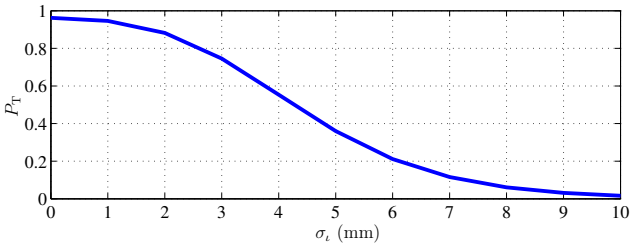

Fig. 2. Total probability of a correct fix for the scenario of Fig. 1 as a function of ionospheric uncertainty σ_ι.

Fig. 1 shows single-epoch, single-frequency results from the analytical ADOP model for parameters that, while still optimistic, more accurately reflect the mass-market use case. The key parameter σ_ϕ is set to 3 mm, and σ_ρ and the elevation cutoff are set to 50 cm and 15 degrees, respectively. The

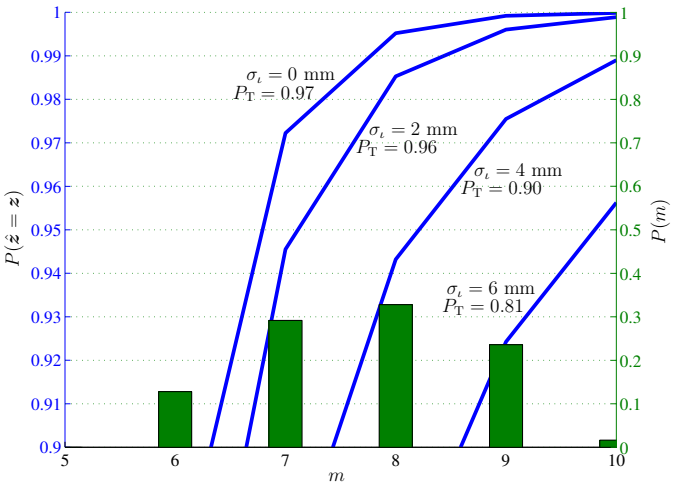

Fig. 3. As Fig. 2 except for dual-frequency (L1-L2) measurements and the probability mass function $P(m)$ corresponds only to a constellation of 31 GPS satellites. The elevation mask angle is again taken to be 15 degrees. It is assumed that dual-frequency measurements can be obtained from every GPS satellite.

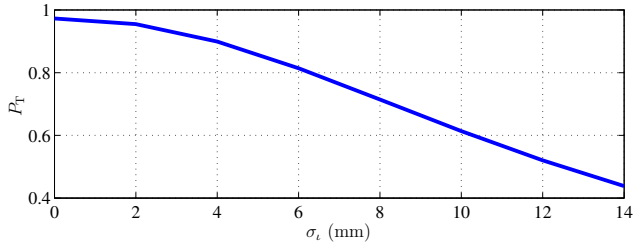

Fig. 4. Total probability of a correct fix for the scenario of Fig. 3 as a function of ionospheric uncertainty σ_ι.

geometry factor f_g is set to 2.5, which is conservative [14] and thus well suited for use cases with strong multipath at low elevation angles. The blue traces in Fig. 1 show $P(\hat{z} = z)$ as a function of m for various values of σ_ι. The green bars represent the probability mass function $P(m)$, or the probability that exactly m satellites will, on average, be above the elevation mask and thus visible to the user. The $P(m)$ shown corresponds to the L1 signals a user in the central United States would see in late 2018, at which point one expects 31 GPS, 14 Galileo, and 3 WAAS satellites.

For each blue trace, the total probability P_T, calculated as

$$P_\mathrm{T} = \sum_{m=1}^{\bar{m}} P(\hat{z} = z|m)P(m)$$

is also given, with the limit $\bar{m}$ chosen high enough to ensure that all nonzero elements of $P(m)$ are included. Fig. 2 plots P_T as a function of σ_ι for the same scenario.

Several conclusions can be drawn from Figs. 1 and 2. Most importantly, it is clear that for single-epoch single-frequency AR to be even moderately reliable ($P_\mathrm{T} \geq 0.9$), the ionospheric uncertainty σ_ι must be held to under 2 mm. Reducing σ_ι from 2 to 1 mm significantly reduces the AR failure rate $(1 - P_\mathrm{T})$—

by more than a factor of two. However, further reduction in σ_ι, even driving it to zero, brings only minor failure rate improvement. For $\sigma_\iota > 2$ mm, single-epoch, single-frequency AR performance will be quite poor, becoming hopeless beyond $\sigma_\iota = 10$ mm.

Figs. 3 and 4 offer results for a dual-frequency (L1-L2) single-epoch scenario. All other scenario parameters are held as for the single-frequency scenario except that, in an attempt to be somewhat more pessimistic, $P(m)$ is based only on GPS satellites. It is assumed that from each satellite the user can extract dual-frequency measurements. Of course, if dual-frequency, or even single-frequency, measurements were also available from non-GPS satellites, the results in Figs. 3 and 4 would improve. On the other hand, mass-market dual-frequency receivers may only track the modernized civil GPS signals on L2, which are only available on 19 of 31 GPS satellites as of April 2016. Limiting $P(m)$ to only GPS satellites stakes out a middle ground that should be approximately representative of the mass-market dual-frequency use case from 2016-2020.

As with the single-frequency case, it is evident that dual-frequency P_{T} is strongly dependent on σ_ι. But the dual-frequency case is more forgiving: for $P_{\mathrm{T}} \geq 0.9$, σ_ι can be as large as 4 mm. The linear asymptote of P_{T} with increasing σ_ι in Fig. 4 reflects the dual-frequency model's ability to compensate for ionospheric uncertainty by performing its own estimation of ionospheric delay, taking advantage of the dispersive nature of the ionosphere and of access to dual-frequency measurements. P_{T} improves with smaller σ_ι because less dual-frequency measurement information is "wasted" on estimating the ionospheric delay. This is the fundamental insight of the ionosphere-weighted model [11].

Despite the dual-frequency model's improved tolerance for larger σ_ι, it remains true that significant performance benefits accrue as σ_ι is reduced—down to about 2 mm. One can conclude from Figs. 1 and 3 that, to achieve a respectable single-epoch P_{T} of 0.95 or greater, single-frequency applications will require $\sigma_\iota \leq 1$ mm and dual-frequency applications will require $\sigma_\iota \leq 2$ mm.

III. Relating Corrections Uncertainty to Network Density

A key question arises in connection with σ_ι: How is σ_ι related to reference network density? One expects σ_ι to decrease with increased network density, but what is the exact relationship?

Ref. [11] adopts a linear relationship between σ_ι and the distance l between the user and the nearest reference station:

$$\sigma_\iota = \beta l, \quad 0.3 \leq \beta \leq 3 \text{ mm/km}$$

Parameter β depends on ionospheric activity; [11] recommends determining β empirically. Similarly, [13] and [14] adopt a linear relation, with $\beta = 0.4$ mm/km. But there appears to be no justification for applying this linear model to ionospheric corrections provided to a user by a network of reference receivers. The linear trend shown in Fig. 4 of [13] corresponds to individual single-baseline solutions involving a single master reference station without network aiding; it is not representative of how σ_ι varies for a rover within a reference network.

Instead of determining how σ_ι varies throughout a reference network, it will be more useful to consider the spatial variation in the variance of aggregate error in network-provided corrections. The aggregate error variance, denoted σ_ν^2, can be modeled as the sum of variances associated with (1) residual ionospheric delay error, (2) residual neutral atmospheric (hereafter tropospheric) error, and (3) error due to carrier-phase multipath at the reference network stations:

$$\sigma_\nu^2 = \sigma_\iota^2 + \sigma_t^2 + \sigma_m^2$$

This model assumes that precise orbital ephemerides are used to eliminate spatially-correlated errors due to satellite ephemeris errors and that the contribution to σ_ν^2 from reference station carrier-phase thermal noise is negligible compared to reference station carrier-phase multipath error.

Taking σ_ν, instead of σ_ι, as the factor of interest—the one to be related to network density—is motivated by an acknowledgment that, in practical application, *any* error in network-provided corrections will degrade AR performance. For single-frequency application of the analytical AR model in [12], exploited in the foregoing section, one has only to substitute σ_ν for σ_ι to properly account for the additional effects of residual tropospheric error and network-side multipath errors in the corrections data. Thus, on the horizontal axis of Fig. 2, σ_ν can be directly substituted for σ_ι.

For dual-frequency application of the analytical AR model, the situation is not so simple: a dual-frequency ionosphere-weighted model can overcome a large σ_ι by estimating the ionospheric delay independently from the network, whereas it can do nothing to reduce the deleterious effects of large σ_t and σ_m. Nonetheless, for the short AR convergence times of interest in this paper (ideally, single-epoch convergence), substituting σ_ν for σ_ι—even in the dual-frequency model—is a valid approximation. This is because, for rapid AR convergence, σ_ι must be small (approximately 2 mm or less), which means that very little information from the rover's dual-frequency measurements is actually directed to the estimation of the residual ionospheric errors. Thus, it is also reasonable to substitute σ_ν for σ_ι on the horizontal axis of Fig. 4.

Focusing therefore on σ_ν, consider its relationship to reference network density γ, expressed in stations per unit area. This relationship depends on the assumed model for the DD ionospheric and tropospheric delays. Let a denote the master reference station and let $\mathcal{S} = \{s_1, s_2, ..., s_N\}$ denote the set of all secondary stations available in the network. Then, for pivot satellite i and alternate satellite j, suppose that the true combined DD atmospheric delay at secondary station $s \in \mathcal{S}$ can be accurately modeled as follows, where x_s, y_s, and z_s represent the secondary station's east, north, and up displacement from the master:

$$\nu_{as}^{ij} = c_x^{ij} x_s + c_y^{ij} y_s + c_z^{ij} z_s + c_0^{ij} \tag{1}$$

Dai et al. refer to this model as a linear interpolation model or first-order surface model [16]. The quantities $c_x^{ij}, c_y^{ij}, c_z^{ij}$ and c_0^{ij} are the model parameters for the satellite pair i, j.

Assuming all reference station antenna locations are perfectly known, the measurement model for a DD carrier-phase residual for the satellite pair i, j, master station a, and secondary station $s \in \mathcal{S}$ is

$$\tilde{\nu}_{as}^{ij} = \nu_{as}^{ij} + w_{a\star}^{ij} + w_{\star s}^{ij} \tag{2}$$

where ν_{as}^{ij} is the true value of the DD atmospheric delay, $w_{a\star}^{ij}$ is the measurement error due to carrier-phase multipath at the master station, and $w_{\star s}^{ij}$ is the measurement error due to carrier phase multipath at the secondary station; $w_{a\star}^{ij}$ and $w_{\star s}^{ij}$ are assumed to be zero mean.

Carrier-phase residuals $\tilde{\nu}_{as}^{ij}$ from all $s \in \mathcal{S}$ can be combined in a least-squares cost function to estimate the parameters c_x^{ij}, c_y^{ij}, c_z^{ij}, and c_0^{ij}, as will be detailed in the next section. An estimate of the DD atmospheric delay at some location x, y, z can then be produced as

$$\hat{\nu}_a^{ij} = \hat{c}_x^{ij} x + \hat{c}_y^{ij} y + \hat{c}_z^{ij} z + \hat{c}_0^{ij}$$

where $(\hat{\cdot})$ denotes estimated parameters. The quantity $\hat{\nu}_a^{ij}$ is modeled as relating to the true DD atmospheric delay ν_a^{ij} at the designated location by

$$\hat{\nu}_a^{ij} = \nu_a^{ij} + w_\nu^{ij}$$

The error term w_ν^{ij} is the aggregate error term discussed previously; it is modeled as having zero mean and variance $2\sigma_\nu^2$ (the factor of two arises because σ_ν^2 is meant to refer to an undifferenced error variance, whereas w_ν^{ij} is a DD error).

The value of σ_ν^2 can be found as a by-product of the least-squares technique; it depends on (1) the geometry of the reference network (the number and locations of secondary reference stations with respect to the master), (2) the statistics of $w_{\star s}^{ij}$, $s \in \mathcal{S}$ (including correlation between these), and (3) the location x, y, z. Note that, importantly, σ_ν^2 is not affected by $w_{a\star}^{ij}$. This is because the non-homogeneous parameter c_0^{ij} in (1) absorbs $w_{a\star}^{ij}$ in the least squares optimization, since $w_{a\star}^{ij}$ is common to all DD carrier-phase residuals $\tilde{\nu}_{as}^{ij}$, $s \in \mathcal{S}$.

Assuming the master and secondary reference station geometry shown in Fig. 5, and assuming uncorrelated, identically-distributed $w_{a\star}^{ij}$ and $w_{\star s}^{ij}$, $s \in \mathcal{S}$, Fig. 5 shows an example map of σ_ν along the x and y axes.

For the linear model in (1), one can show that if stations are sufficiently uniformly distributed (i.e., no station clumping), then the average value of σ_ν across a network, denoted $\bar{\sigma}_\nu$, is approximately related to the network density γ by

$$\bar{\sigma}_\nu = \frac{q}{\sqrt{\gamma}} \tag{3}$$

where q is a parameter related to the variance of the uncorrelated errors $w_{\star s}^{ij}$, $s \in \mathcal{S}$. This approximation becomes highly accurate as γ increases.

It is clear from (3) that, for the linear model (1), $\bar{\sigma}_\nu$ can be driven to an arbitrarily small value by increasing the network density γ, and this is true despite the presence of multipath in the reference station carrier-phase measurements. Whether (3) applies in practice depends on whether (1) can be considered an accurate model for ν_{as}^{ij}, at least over a compact region. The following section examines this question empirically. It further seeks to identify, for an example dense reference network, the density γ beyond which further reduction in $\bar{\sigma}_\nu$ no longer matters (would no longer improve $P(\hat{\boldsymbol{z}} = \boldsymbol{z})$) because rover multipath dominates.

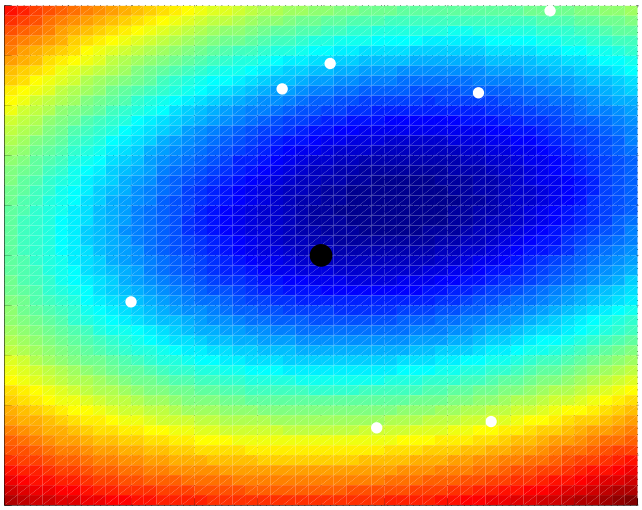

Fig. 5. Map showing trends in σ_ν across a simulated reference network assuming a linear model for combined DD ionospheric and tropospheric delays and independent errors due to multipath at each station. The master station is marked in black; secondary reference stations are marked in white. Blue denotes low σ_ν; red denotes high σ_ν.

IV. Analysis of a Dense Reference Network

A. Data selection and processing

An analysis of dense reference network performance was conducted using data from several organizations providing GNSS reference station observations; namely, NGS CORS (National Geodetic Survey Continuously Operating Reference Stations), UNAVCO, and CRTN (California Real Time Network). This combination of sources allowed analysis of a hypothetical reference network of 23 high-quality GNSS receivers with an overall network density of approximately 8 nodes/1000 km^2 or, alternately expressed, an average inter-station spacing of 14 km. The sites selected to comprise this reference network, located between Los Angeles, CA and Pomona, CA, are listed in Table I and their relative positions are depicted graphically in Fig. 6.

All available GPS L1 C/A data from GPS weeks 1850 through 1859 were used for the analysis. Double-differencing of carrier-phase observations was used exclusively. Station LONG was maintained in every combination as the master reference station. The highest elevation satellite for each solution window was selected as the pivot satellite. A minimum satellite elevation mask was enforced at 20 degrees. Additionally, any

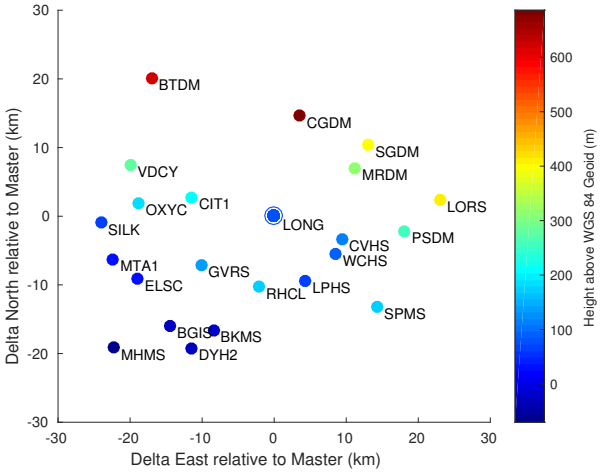

Fig. 6. Depiction of the placement of the 23 GNSS reference stations listed in Table I. Horizontal positions are relative to the master station, LONG of CRTN, in kilometers. The color map indicates the height of each station above the WGS 84 geoid in meters.

TABLE I
SELECTED REFERENCE STATIONS FOR ANALYSIS

Station ID	Network	Distance to Master (km)
LONG	CRTN	Master
CVHS	CRTN	10.0
WCHS	CRTN	10.2
LPHS	UNAVCO	10.4
RHCL	CRTN	10.5
CIT1	CRTN	11.8
GVRS	CRTN	12.4
MRDM	UNAVCO	13.2
CGDM	UNAVCO	15.1
SGDM	UNAVCO	16.7
PSDM	CRTN	18.3
BKMS	UNAVCO	18.6
OXYC	CRTN	18.9
SPMS	UNAVCO	19.5
ELSC	CRTN	21.0
VDCY	CRTN	21.3
BGIS	UNAVCO	21.6
DYH2	UNAVCO	22.4
LORS	CORS	23.1
MTA1	UNAVCO	23.2
SILK	UNAVCO	24.1
BTDM	UNAVCO	26.3
MHMS	CRTN	29.4

satellite not above the elevation mask and providing carrier-phase observations at both the beginning and end of any given processing window was excluded. A step size of 10 minutes was used. The longest available sub-window, meeting the above requirements and providing a minimum of 6 satellite vehicles (1 pivot satellite and 5 others), was selected for processing. To facilitate batch processing, integer ambiguities were assumed to have resolved correctly when the mean standard deviation of carrier-phase residuals for that solution was less than one quarter wavelength of the GPS L1 frequency. In application, this final constraint resulted in rejecting only 0.6% of all solutions.

B. Network corrections estimation

Estimation of network corrections made use of least-squares estimation applied to carrier-phase residuals measured between master station LONG, denoted a hereafter, and secondary reference stations $s \in \mathcal{S}$, where $\mathcal{S}$ is now taken to be the set of all stations other than LONG in Table I. Consider the following model for the DD carrier-phase measurement, expressed in meters, between master station a, secondary station $s \in \mathcal{S}$, pivot satellite i, and alternate satellite j:

$$\lambda\phi_{as}^{ij} = r_{as}^{ij} + \nu_{as}^{ij} + \lambda N_{as}^{ij} + w_{as}^{ij} \tag{4}$$

Here, λ is the carrier wavelength; ϕ_{as}^{ij} is the DD carrier-phase measurement, in cycles; r_{as}^{ij} is the DD range; $N_{as}^{ij} \in \mathbb{Z}$ is the DD integer ambiguity; ν_{as}^{ij} is the DD combined atmospheric delay, which includes tropospheric and ionospheric delays; and w_{as}^{ij} is the DD carrier-phase measurement error, which is dominated by carrier-phase multipath error at a and s.

Experimental analysis of $\bar{\sigma}_\nu$ as a function of network density proceeded as follows. A subset of secondary stations $\mathcal{S}_k \subset \mathcal{S}$ was chosen, together with a, to act as the kth test network. A large number K of subsets $\mathcal{S}_k$ of various geographic size and density were analyzed. Let $\{\mathcal{S} \setminus \mathcal{S}_k\}$ denote the set of secondary stations not in the kth test network. For each $\mathcal{S}_k,\ k = 1, 2, \ldots, K$, all secondary stations in $\{\mathcal{S} \setminus \mathcal{S}_k\}$ were designated, one at a time, to act as a test station, or rover. Atmospheric delays estimated by the kth network for test station $s \in \{\mathcal{S} \setminus \mathcal{S}_k\}$ were then differenced from actual delays measured by s to evaluate the quality of the atmospheric delay estimates.

Details of the atmospheric delay estimation procedure for the kth test network are as follows. For each $s \in \mathcal{S}_k$, a DD measurement residual was formed for each pivot satellite i and alternate satellite j as

$$\tilde{\nu}_{as}^{ij} = \lambda\phi_{as}^{ij} - r_{as}^{ij} - \lambda N_{as}^{ij} \tag{5}$$

where r_{as}^{ij} was assumed known to sub-millimeter accuracy and N_{as}^{ij} was assumed to have been resolved correctly. The true DD atmospheric error ν_{as}^{ij} contributing to (5) was assumed to vary linearly with geometry over sufficiently short baselines as modeled in (2). The DD multipath error term w_{as}^{ij} was assumed to be zero mean, and the component $w_{\star s}^{ij}$ due solely to s was assumed to be uncorrelated with all corresponding components $w_{\star u}^{ij},\ u \in \{\mathcal{S}_k \setminus s\}$.

Under these assumptions, ν_{as}^{ij} can readily be estimated via least squares. Let $\tilde{\boldsymbol{\nu}}^{ij}$ be the $|\mathcal{S}_k| \times 1$ vector containing the residuals $\tilde{\nu}_{as}^{ij}$ for $s \in \mathcal{S}_k$. This residuals vector can be modeled as

$$\tilde{\boldsymbol{\nu}}^{ij} = H\mathbf{c}_1^{ij} + \mathbf{w}^{ij} \tag{6}$$

where H is an $|\mathcal{S}_k| \times 4$ matrix whose rows are of the form $[x_s \quad y_s \quad z_s \quad 1]$. The 4×1 vector

$$\mathbf{c}_1^{ij} = [c_{x1}^{ij}, c_{y1}^{ij}, c_{z1}^{ij}, c_0^{ij}]^T$$

contains the parameters of the hyper-plane to be estimated at each epoch. The $|\mathcal{S}_k|\times 1$ vector $\mathbf{w}^{ij}$ contains DD measurement errors.

An estimate $\hat{\mathbf{c}}_1^{ij}$ from a least-squares solution of (6) was used to produce a network correction $\hat{\nu}_{as}^{ij}$ for a test secondary station $s \in \{\mathcal{S} \setminus \mathcal{S}_k\}$, acting as rover, at location x_s, y_s, z_s:

$$\hat{\nu}_{as,l}^{ij} = \hat{c}_{x1}^{ij} x_s + \hat{c}_{y1}^{ij} y_s + \hat{c}_{z1}^{ij} z_s + \hat{c}_0^{ij} \tag{7}$$

The subscript l on the atmospheric correction $\hat{\nu}_{as,l}^{ij}$ indicates that the correction is based on a linear model for DD atmospheric errors; it is used to distinguish the correction from those produced by a quadratic model later on. The correction $\hat{\nu}_{as,l}^{ij}$ was applied at test station $s \in \{\mathcal{S} \setminus \mathcal{S}_k\}$ to produce a corrected DD phase measurement

$$\lambda\tilde{\phi}_{as}^{ij} = \lambda\phi_{as}^{ij} - \hat{\nu}_{as}^{ij}$$

This procedure was repeated at each epoch for each satellite pair i, j visible to each test station $s \in \{\mathcal{S} \setminus \mathcal{S}_k\}$ of the kth test network, $k = 1, 2, ..., K$.

If the assumed models hold, then in the limit as the network density increases, $\lambda\tilde{\phi}_{as}^{ij}$ can be modeled as

$$\lambda\tilde{\phi}_{as}^{ij} = r_{as}^{ij} + \lambda N_{as}^{ij} + w_{\star s}^{ij} \tag{8}$$

where $w_{\star s}^{ij}$ is DD phase measurement error due only to multipath at s. In other words, as network density increases, application of the network correction $\hat{\nu}_{as,l}^{ij}$ eliminates not only ν_{as}^{ij} but also $w_{a\star}^{ij}$, the component of the DD phase measurement error due to multipath at the master.

C. Linear least-squares compared to quadratic-least squares estimation

To evaluate the assumption that DD tropospheric and ionospheric errors vary proportional to relative position, $\mathbf{c}_1$ was estimated with the full set of secondary stations $\mathcal{S}$ for single epochs at 300 second intervals. The probability distributions of the contributions of those parameters (e.g., $c_{x1}x_s$ and not simply c_{x1}) are shown in Fig. 7. For comparison, equivalent values are calculated for a quadratic least-squares estimate of the following form:

$$\begin{aligned}\hat{\nu}_{as,q}^{ij} = {} & \hat{c}_{x2}^{ij} x_s^2 + \hat{c}_{y2}^{ij} y_s^2 + \hat{c}_{z2}^{ij} z_s^2 \\ & + \hat{c}_{x1}^{ij} x_s + \hat{c}_{y1}^{ij} y_s + \hat{c}_{z1}^{ij} z_s + \hat{c}_0^{ij}\end{aligned} \tag{9}$$

Here, the subscript q of $\hat{\nu}_{as,q}^{ij}$ denotes a quadratic model for DD atmospheric delays. The distributions of comparable terms from (9) are also shown in Fig. 7 and 8. These data represent the collection of all satellites above the elevation mask angle. It is noted that when all satellites are considered together, the expected value of these terms is very near zero.

Fig. 9 and 10 show the same data as Fig. 7 and 8 but with each GPS satellite plotted separately. It is noted that the linear parameters, when considering only a particular satellite, are not necessarily zero-mean. This is hypothesized to be a manifestation of the satellite orbit reflected in the tropospheric and ionospheric errors. It is interesting to note that the quadratic terms shown in Fig. 10 largely exhibit zero

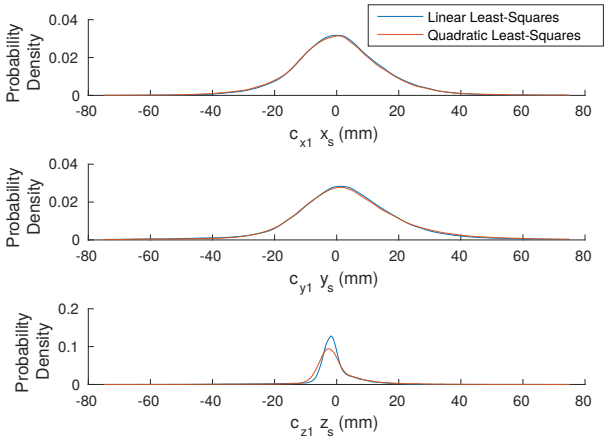

Fig. 7. Probability densities of the $\hat{c}_{x1}x_s$, $\hat{c}_{y1}y_s$, and $\hat{c}_{z1}z_s$ terms estimated at the station location for SPMS of UNAVCO. As indicated by the legend, the linear components are shown for a linear least-squares estimation as well as the linear components for a quadratic least-squares estimation. These data represent the probability densities for all GPS satellites combined.

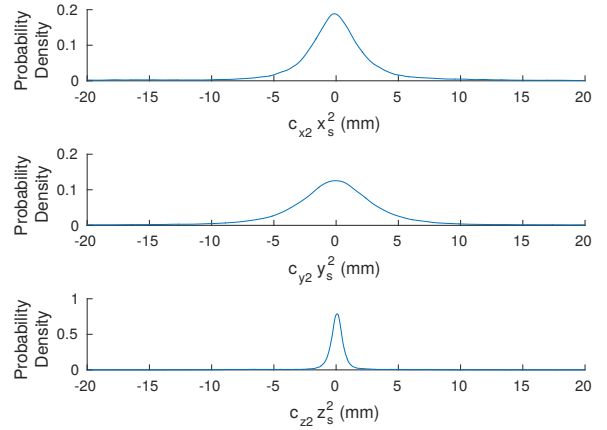

Fig. 8. Probability densities of the $\hat{c}_{x2}x_s^2$, $\hat{c}_{y2}y_s^2$, and $\hat{c}_{z2}z^2$ terms calculated at the station location for SPMS of UNAVCO.

mean behavior despite non-zero mean for the associated linear terms.

Fig. 11 shows the probability distributions of the difference between (7) and (9) (i.e., $\hat{\nu}_{as,l}^{ij} - \hat{\nu}_{as,q}^{ij}$) at 3 representative reference station positions. It can be noticed that despite the increasing baseline distance of LORS and BGIS as compared to CGDM, there is no apparent correlation in these estimation errors. Notice that CGDM and LORS have very similar distributions despite their difference in baselines. BGIS and LORS, with similar baselines, exhibit very different distributions. There is no apparent correlation found between reference station positions and these error terms. Additionally, these distributions are zero-mean for all $s \in \mathcal{S}$ (to within 0.5 mm in each case) with 68.27% boundaries (see Fig. 11 caption for an explanation) positioned between $1.5 - 5.5$ mm. Because these errors appear indistinguishable from multipath, it is concluded,

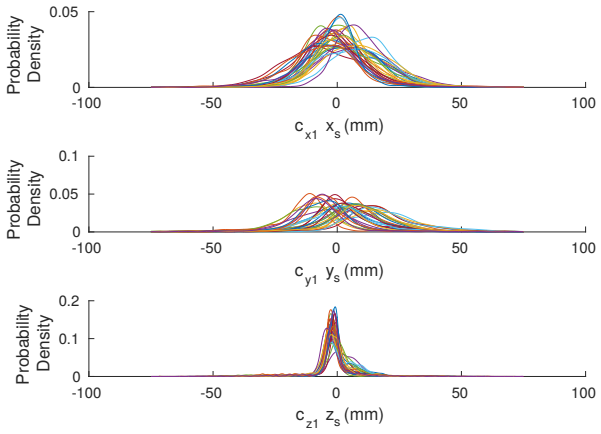

Fig. 9. Probability densities of the $\hat{c}_{x1}x_s$, $\hat{c}_{y1}y_s$, and $\hat{c}_{z1}z_s$ terms for every GPS satellite observed, calculated at the station location for SPMS of UNAVCO, where each plot line represents a different GPS satellite. This figure is intended to qualitatively illustrate the non-zero mean nature of these linear terms when considered for individual satellites.

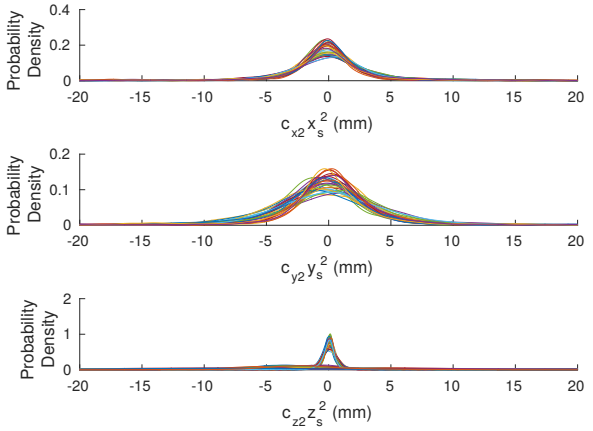

Fig. 10. Probability densities of the $\hat{c}_{x2}x_s^2$, $\hat{c}_{y2}y_s^2$, and $\hat{c}_{z2}z_s^2$ terms for every GPS satellite observed, calculated at the station location for SPMS of UNAVCO, where each plot line represents a different GPS satellite. This figure is included to qualitatively illustrate the largely zero mean nature of these quadratic terms when considered for individual satellites.

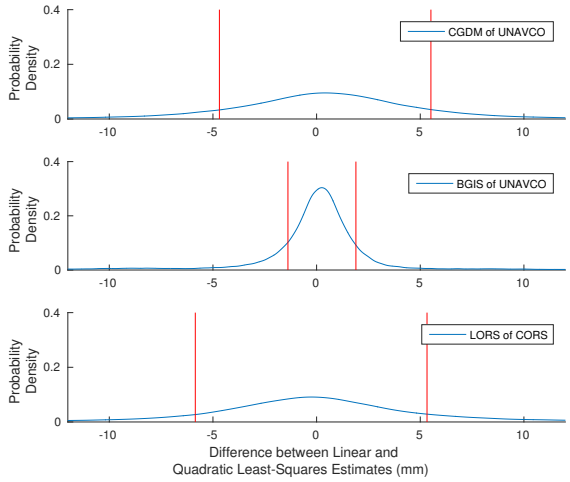

Fig. 11. Probability densities of the difference between linear least-squares and quadratic least-squares network correction estimates ($\hat{\nu}^{ij}_{as,l} - \hat{\nu}^{ij}_{as,q}$) for representative reference stations. The red vertical lines denote boundaries between which 68.27% of the probability distribution is contained; displayed as a comparative proxy to 1σ of the Gaussian-distribution (these distributions are non-Gaussian). Recall that CGDM has a distance to the master station of 15.1km, BGIS is at 21.6km, and LORS is at 23.1km.

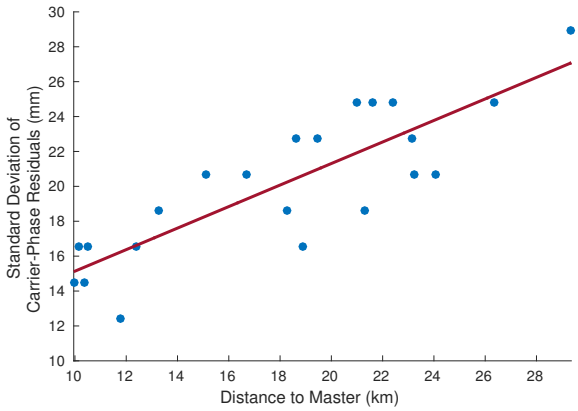

Fig. 12. Standard deviation of uncorrected DD carrier-phase residuals versus baseline distance between each of the 22 reference stations and the master reference station. The fitted curve has an equation of $\nu^{ij}_{as}(r_{as}) = 0.62r_{as}+9$ which suggest a linear growth of DD tropospheric and ionospheric errors of $\beta = 0.62\text{mm/km}$ for this set of data.

for this specific network and time period, that linear least-squares estimation is sufficient for estimating tropospheric and ionospheric errors. This is fortunate, because the linear model for atmospheric DD delays provides an averaging effect on multipath present at the reference stations which minimizes the introduction of multipath errors into the estimates produced.

D. Uncorrected carrier-phase residuals

Fig. 12 shows the expected values for DD carrier-phase residual standard deviations for all $s \in \mathcal{S}$ through use of uncorrected observations. These data were produced by averaging the standard deviation of the DD carrier-phase residuals calculated at each epoch across all satellites present in the solution. The fitted curve indicates a linear growth of DD carrier-phase residuals with $\beta = 0.62$ mm/km. Additionally, the mm-level scatter of these data points suggest that position biases of the resolved reference station positions are also mm-level. If the linear fit is shifted down by approximately 4 mm (e.g., taking the minimum data points as those with very little position bias) and extrapolated to 0 km, one can consider this as providing a rough estimate of DD multipath at the reference stations; 4.7 mm (DD) or 3.3 mm (single-difference equivalent).

E. Network corrected carrier-phase residuals

1) Network generation and processing: Fig. 13 displays similar data to those shown in Fig. 12. These carrier-phase

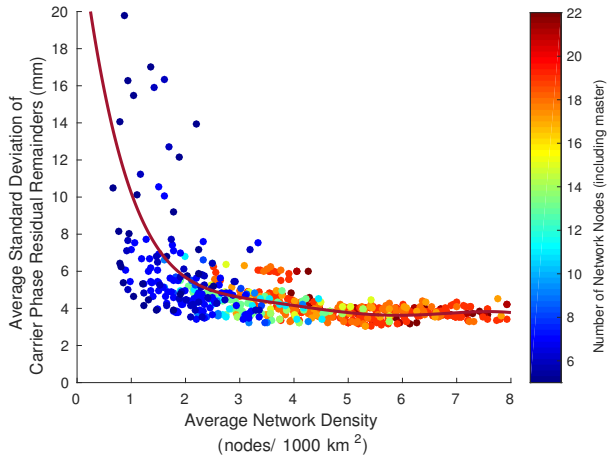

Fig. 13. Standard deviation of carrier-phase residual remainders (the carrier-phase residuals which remain after application of network corrections) versus average network density. The fitted curve is simply a polynomial fit of these data whose selection is not based on any theoretically anticipated behavior.

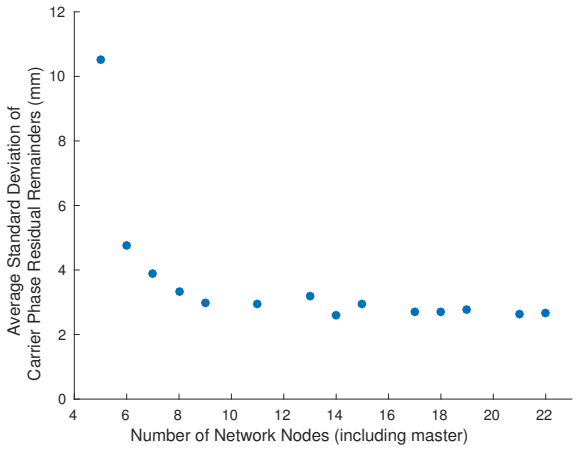

Fig. 14. Standard deviation of carrier-phase residual remainders (the carrier-phase residuals which remain after application of network corrections) versus the number of network nodes (including master).

residual values are what remain after application of network corrections produced as detailed in Section IV-B. Each data point corresponds to a particular subset of secondary stations $\mathcal{S}_k \subset \mathcal{S}$, together with a, and a particular rover selected from $\{\mathcal{S} \setminus \mathcal{S}_k\}$. For each $\mathcal{S}_k$, $k = 1, 2, \ldots, K$, both the size and specific selection of secondary stations comprising that subset were randomly selected. In all, 70 different network configurations (i.e., $K = 70$) and over 3.67 million NRTK solutions were analyzed.

2) Average network density metric: The horizontal-axis utilizes a metric intended to represent an average network density relative to the rover of those reference stations used to estimate network corrections for a given plotted data point. Average network density is calculated as the average value of all iterates $\frac{N(r)}{\pi r^2}$ for r^2 from $r^2_{\min}$ to $r^2_{\max}$. $N(r)$ is the integer quantity of network reference stations within distance r of the rover. $r_{\min}$ and $r_{\max}$ are distances to the nearest and farthest references stations, respectively, relative to the rover.

3) Discussion of results: It is seen in Fig. 13 that carrier-phase residuals after application of network corrections are, in most cases, considerably reduced compared to those original magnitudes seen in Fig. 12. Few network configurations of ≤ 6 nodes demonstrate comparable performance to the best performing network configurations. In fact, where networks of ≥ 13 nodes have a mean value of 2.8 mm and a maximum value of 4.9 mm, the mean value for all networks of ≤ 6 nodes is 6.4 mm with several considerably larger values beyond that.

Fig. 13, with increasing network density, appears to asymptotically approach a minimum value of 4 mm. Even for hypothetical perfect network corrections, single-difference (between satellites) multipath from the rover will persist in these residuals. Recall the previous rough estimate for single-difference multipath of these reference stations of 3.3 mm. These results suggest that network densities beyond 5 nodes/1000 km^2 provide remaining correction errors of < 2 mm (e.g., the margin between the asymptote and the attributed rover multipath level).

4) Recommendations: From Fig. 13 it can be seen that average network densities beyond 5 nodes/1000 km^2 provide negligible improvement in reducing carrier-phase residuals once σ_ν is reduced below the floor of rover multipath. *This equates to a maximum recommended station spacing of* 18 *km for a uniformly-spaced network.* Fig. 14 shows diminishing returns at around 10 network nodes, yet these data do show an additional improvement of 0.3 mm between 11 and 22 network nodes. Additional nodes should be included beyond these recommendations to provide redundancy.

V. Development of a Dense Reference Network in Austin

A low-cost reference network testbed is being developed and deployed by the University of Texas at Austin around the city of Austin, Texas. Sites for station deployment, including building rooftops and illumination poles, have been provided by the Texas Department of Transportation. Fig. 15 shows one of the network's low-cost reference stations.

The testbed will be useful for investigating how the 18-km inter-station-spacing recommendation scales to a dense network of low-cost reference stations in environments with greater multipath and signal blockage than those of the sites studied in the foregoing section (the high-quality permanently-operating stations listed in Table I). Such non-ideal signal environments are to be expected in a dense low-cost reference network, for which choice of station siting is driven largely by opportunity.

The reference station design is novel. Each station is a self-contained, self-powered node supporting a software-defined dual-frequency, dual-antenna GNSS receiver with an always-on cellular connection to university servers for data collection

Fig. 15. A low-cost reference station in the University of Texas at Austin reference network, deployed in March, 2016, in Austin, Texas.

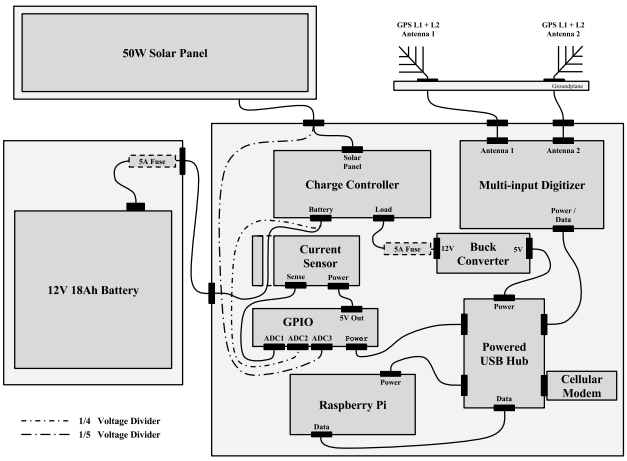

Fig. 16. Reference station components diagram.

and software maintenance. The stations can be broken down into four functional elements: the structure, power system, GNSS receiver, and communication system.

A. Reference stations

1) Physical structure: The frame of the reference station, constructed out of 80/20 aluminum extrusion, is configured such that the angle between the legs may be adjusted to optimize the angle of the solar panel mounted to the front legs. 60-degree inside-angle brackets mounted atop the front legs provide a secure, level connection of the antenna ground plane in a position such that it can protect the antennas from multipath reflecting off of the structure and prevent casting shadows onto the solar panel. An angle of 60 degrees (from ground) has been chosen to optimize solar power during the short days of the winter months in Austin, Texas. Alternate angle brackets may be used to mount the ground plane at different angles of deployment. Two NEMA-certified weather-sealed plastic electrical boxes attached to the legs of the frame house the battery and electronics. Also in development is a similarly-constructed pole-mount station, configured to be easily mounted on existing city infrastructure, such as illumination poles.

2) Communications and processing: Data management and communication is performed by a Raspberry Pi 2 Model B. The Raspberry Pi connects to a USB hub that provides both power and a data interface to other components. These include a Huawei cellular modem, a dual-input GNSS signal digitizer, and an 8-channel GPIO/ADC board. The Raspberry Pi utilizes the cellular modem to communicate data to the network server at a 1-second data interval and allows remote access via a reverse SSH tunnel. A reverse SSH tunnel is necessary since the cellular provider assigns a dynamic IP address and enforces a restrictive firewall on clients.

3) Receiver hardware: The dual-frequency (L1-L2) GNSS receiver draws radio frequency signals from two Tallysman TW3870 dual-frequency antennas mounted to a 6”$\times$2’$\times$1/4” aluminum backplane with a relative baseline between antennas of 18”. Antenna-to-receiver connections are achieved through TNC-to-TNC cables connected to bulkhead TNC-to-MMCX assemblies at the electronics box. The dual-input GNSS signal digitizer receives power from the USB hub and outputs two-bit-quantized GNSS sample data at 19.2 MHz (at each of L1 and L2) through the USB hub. GNSS signal processing is performed by GRID, an in-house-developed software defined receiver [17]–[19], which runs in real time on the Raspberry Pi.

4) Power system: The reference stations are completely self-sustaining, drawing power from a 50-Watt polycrystalline solar panel and a 12-Volt, 18-Amp-hour, sealed lead-acid battery. On a full charge, the battery is sized to sustain full operation of the reference station for 48 hours. The solar panel is sized to replenish 24 hours of power consumption from 2 hours of full sunlight.

Battery charging is controlled by a 5-Amp PWM (pulse-width modulated) charge controller. A 12VDC-to-5VDC, 3-Amp buck converter provides regulated power to a 4-port 2.5-Amp USB 2.0 hub. The powered USB hub serves as a USB breakout for the Raspberry Pi, providing component protection and isolation as well as supplying the power demands of all the USB-powered peripherals. Total power draw when operational and transmitting observations at a 1-second interval is approximately 4.1 Watts.

Inline fuses are installed on the buck converter input and the battery. Power system monitoring and logging of battery voltage, battery current, and solar panel voltage is implemented through the combination of voltage dividers, a Hall-effect current sensor, and an 8-channel GPIO/ADC-to-USB board.

B. Network Layout

Initial deployment of this reference network has begun with rooftop installation of 9 reference stations to Texas Department of Transportation, University of Texas, and private facilities. In anticipation of a benefit to public transportation safety

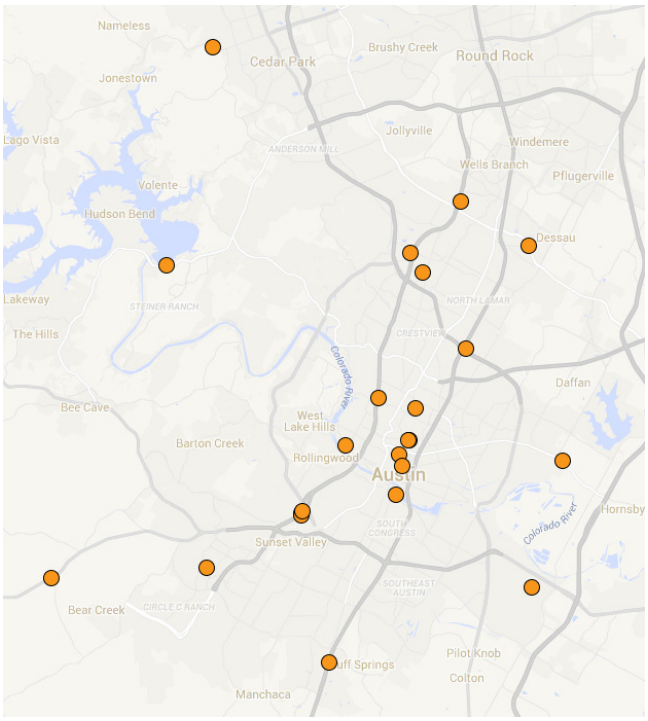

Fig. 17. Map overview of the planned Austin area reference network (Google Maps).

and the "connected city" future, the Texas Department of Transportation has agreed to contribute rooftop access to a total of 11 facilities for rooftop stations and 3 illumination pole mount locations for pole-mount stations. All together, current plans are for 20 reference stations throughout the city of Austin. Fig. 17 shows the first selection of deployment locations. Full deployment is to be completed by June, 2016. The reference network's average inter-station spacing is far shorter than the 18-km recommendation of Section IV-E4. The tighter spacing provides redundancy and flexibility of experimentation.

VI. Conclusions

For a sufficiently dense reference network, linear least squares estimation can be applied to the task of reducing uncertainties due to tropospheric and ionospheric delays for the purposes of providing improved positioning accuracy as well as faster time to ambiguity resolution for carrier-phase differential positioning. High network density allows use of a strong linear model for atmospheric delays, which has the virtue of suppressing network-side multipath errors in the provided corrections.

A network of 23 high-quality reference stations in the vicinity of Los Angeles, California was studied to determine what network density is sufficient to make all network-side error sources negligible compared to rover receiver multipath. A density of $\geq$5 stations per 1000 km^2, or an average inter-station spacing of $\leq$18 km, was found to drive network-side ionospheric, tropospheric, and multipath errors well below rover receiver multipath.

These findings motivate a 5- to 25-fold densification of existing permanent reference networks to support mass-market applications for which low user (rover receiver) cost and rapid convergence to a reliable sub-decimeter position are a priority. A dense network of low-cost reference stations is being deployed in Austin, Texas, by the University of Texas at Austin, in collaboration with the Texas Department of Transportation, to further explore the benefits of high-density GNSS reference networks for mass-market precise positioning.

Acknowledgments

This work was supported in part by the Data-Supported Transportation Operations and Planning Center (D-STOP), a Tier 1 USDOT University Transportation Center, and by the Texas Department of Transportation under the *Connected Vehicle Problems, Challenges and Major Technologies* project.

Endnote

Author Todd Humphreys is Scientific Advisor to Radiosense, a startup developing technology for low-cost precise positioning.

References

[1] P. Henkel and P. Burger, "Multi-sensor fusion of GNSS receivers, inertial sensor and cameras for precise and reliable positioning," 2015, http://anavs.de/wp-content/uploads/2015/07/HenBur15-COFAT-2015.pdf.

[2] F. Pisoni, G. Avellone, D. Di Grazia, and J. L. Wilson, "Precise positioning and L2C signal reception for the mass market," in *Proceedings of the ION GNSS+ Meeting*, Tampa, FL, 2015.

[3] K. M. Pesyna, Jr., T. Novlan, C. Zhang, R. W. Heath, Jr., and T. E. Humphreys, "Exploiting antenna motion for faster initialization of centimeter-accurate GNSS positioning with low-cost antennas," *IEEE Transactions on Aerospace and Electronic Systems*, 2016, in preparation after favorable reviews.

[4] K. M. Pesyna, Jr., D. P. Shepard, R. W. Heath, Jr., and T. E. Humphreys, "VISRTK: Fusion of camera and GNSS carrier phase measurements for fast, robust, precise, and globally-referenced mobile device pose determination," *IEEE Transactions on Signal Processing*, 2016, in preparation.

[5] A. Jokinen, C. Ellum, J. Neumann, D. Chan, I. Webster, S. Masterson, and T. Morley, "Kinematic performance of novatel CORRECT with TerraStar-D precise point positioning (PPP) service," 2014.

[6] L. Mervart, C. Rocken, T. Iwabuchi, Z. Lukes, and M. Kanzaki, "Precise point positioning with fast ambiguity resolution—prerequisites, algorithms, and performance," in *Proceedings of the ION GNSS+ Meeting*, Nashville, TN, 2013.

[7] S. Banville, P. Collins, W. Zhang, and R. B. Langley, "Global and regional ionospheric corrections for faster PPP convergence," *Navigation*, vol. 61, no. 2, pp. 115–124, 2014.

[8] X. Ren, S. Choy, K. Harima, and X. Zhang, "Multi-constellation gnss precise point positioning using GPS, GLONASS and BeiDou in Australia," in *International Global Navigation Satellite Systems (IGNSS) Symposium*. International Global Navigation Satellite Systems Society, 2015, pp. 1–13.

[9] P. Teunissen and A. Khodabandeh, "Review and principles of PPP-RTK methods," *Journal of Geodesy*, vol. 89, no. 3, pp. 217–240, 2014.

[10] D. Odijk, P. J. Teunissen, and A. Khodabandeh, "Single-frequency PPP-RTK: theory and experimental results," in *Earth on the Edge: Science for a Sustainable Planet*. Springer, 2014, pp. 571–578.

[11] D. Odijk, "Fast precise GPS positioning in the presence of ionospheric delays," Ph.D. dissertation, PhD dissertation, Faculty of Civil Engineering and Geosciences, Delft University of Technology, Delft.

[12] D. Odijk and P. Teunissen, "ADOP in closed form for a hierarchy of multi-frequency single-baseline GNSS models," *Journal of Geodesy*, vol. 82, no. 8, pp. 473–492, 2008.

[13] D. Odijk, "Weighting ionospheric corrections to improve fast GPS positioning over medium distances," in *ION GPS*, 2000, pp. 1113–1123.

[14] S. Verhagen, D. Odijk, P. J. Teunissen, and L. Huisman, "Performance improvement with low-cost multi-GNSS receivers," in *Satellite Navigation Technologies and European Workshop on GNSS Signals and Signal Processing (NAVITEC), 2010 5th ESA Workshop on*. IEEE, 2010, pp. 1–8.

[15] K. M. Pesyna, Jr., R. W. Heath, Jr., and T. E. Humphreys, "Centimeter positioning with a smartphone-quality GNSS antenna," in *Proceedings of the ION GNSS+ Meeting*, 2014.

[16] L. Dai, S. Han, J. Wang, and C. Rizos, "Comparison of interpolation algorithms in network-based GPS techniques," *Navigation, Journal of the Institute of Navigation*, vol. 50, no. 4, pp. 277–293, 2003.

[17] T. E. Humphreys, B. M. Ledvina, M. L. Psiaki, and P. M. Kintner, Jr., "GNSS receiver implementation on a DSP: Status, challenges, and prospects," in *Proceedings of the ION GNSS Meeting*. Fort Worth, TX: Institute of Navigation, 2006, pp. 2370–2382.

[18] T. E. Humphreys, J. Bhatti, T. Pany, B. Ledvina, and B. O'Hanlon, "Exploiting multicore technology in software-defined GNSS receivers," in *Proceedings of the ION GNSS Meeting*. Savannah, GA: Institute of Navigation, 2009, pp. 326–338.

[19] E. G. Lightsey, T. E. Humphreys, J. A. Bhatti, A. J. Joplin, B. W. O'Hanlon, and S. P. Powell, "Demonstration of a space capable miniature dual frequency GNSS receiver," *Navigation, Journal of the Institute of Navigation*, vol. 61, no. 1, pp. 53–64, 2014.